

RESEARCH ARTICLE | NOVEMBER 18 2024

Influence of intensity distributions on the process dynamics during laser deep penetration welding of pure nickel with a flexible ring mode laser source

Special Collection: [Proceedings of the International Congress of Applications of Lasers & Electro-Optics \(ICALEO 2024\)](#)

Marcel Möbus ; Ronald Pordzik ; Thomas Seefeld 



J. Laser Appl. 36, 042073 (2024)

<https://doi.org/10.2351/7.0001529>



Articles You May Be Interested In

Influence of superimposed intensity distributions on weld seam quality and spatter behavior during laser beam welding of copper with green laser radiation

J. Laser Appl. (September 2022)

Influence of ring-shaped beam profiles on spatter characteristics in laser-based powder bed fusion of metals

J. Laser Appl. (September 2023)

Identifying the direction of weld path deviations in laser deep penetration welding of hidden T-joints by means of OCT

J. Laser Appl. (August 2024)

26 March 2025 14:37:02



Influence of intensity distributions on the process dynamics during laser deep penetration welding of pure nickel with a flexible ring mode laser source

Cite as: J. Laser Appl. 36, 042073 (2024); doi: 10.2351/7.0001529

Submitted: 7 June 2024 · Accepted: 11 October 2024 ·

Published Online: 18 November 2024



View Online



Export Citation



CrossMark

Marcel Möbus,^{1,a)}  Ronald Pordzik,¹  and Thomas Seefeld^{1,2} 

AFFILIATIONS

¹BIAS—Bremer Institut für angewandte Strahltechnik GmbH, Klagenfurter Straße 5, Bremen 28359, Germany

²MAPEX Center for Materials and Processes—Universität Bremen, Bibliothekstraße 1, Bremen 28359, Germany

Note: Paper published as part of the special topic on Proceedings of the International Congress of Applications of Lasers & Electro-Optics 2024.

^{a)}Author to whom correspondence should be addressed; electronic mail: moebus@bias.de

ABSTRACT

Current research results demonstrate the potential of spatter reduction in laser deep penetration welding by using adapted laser beam intensity distributions between a ring and a core intensity. The spatter-reducing effect, resulting from the additional ring intensity, is often attributed to an enlarged keyhole opening. However, it remains a matter of debate how exactly an additional ring intensity influences the process. This study, therefore, investigates the effect of an increasing ring intensity on process dynamics and the spatter formation regime. Laser beam welding experiments were carried out on 2.4068 nickel hidden T-joints at different welding speeds of up to 16 m/min, as well as different intensity distributions, while maintaining a constant weld depth. The tests were evaluated by using two high-speed cameras from different angles to analyze spatter and their formation mechanisms as well as the keyhole opening. Metallographic analyses and x-ray images were used to determine influences on the seam shape and porosity. It was shown that a change in intensity distribution has a significant influence on the melt flow, the resulting amount of spatter, and the porosity, which is comparable across the investigated welding speeds. While a core-based power distribution leads to spatter formation on the rear of the keyhole opening, it was shown that a ring-based power distribution leads to spatter formation on both sides of the keyhole. With an optimal power distribution, spatter formation could be largely prevented. Based on these findings, the single wave regime, a stabilized regime, and a lateral spatter regime were identified.

Key words: laser welding, intensity distribution, welding speed, spatter, porosity

© 2024 Author(s). All article content, except where otherwise noted, is licensed under a Creative Commons Attribution (CC BY) license (<https://creativecommons.org/licenses/by/4.0/>). <https://doi.org/10.2351/7.0001529>

I. INTRODUCTION

Laser deep penetration welding of various materials has proven to be a fast and high-quality welding process and is widely used wherever large quantities are achieved through a high degree of automation. This process is also essential for green energy transition, e.g., for the production of hydrogen generation technologies. In order to meet the rising hydrogen demand, a growth of generation facilities by more than 200 % per year is required between the years 2025 and

2030.¹ This also necessitates an increase in the productivity of the laser welding process. Simply increasing the welding speed can lead to unsteady processes characterized by spatter and pores, depending on the process regime.² Recent studies have shown that these process instabilities can be significantly reduced for various metals such as steel,³ aluminum,^{4,5} copper,⁶ titanium alloys,⁷ and dissimilar weld materials like Al-Cu⁸ by using flexible ring mode (FRM) laser sources with both infrared and visible wavelengths.⁹

26 March 2025 14:37:02

The reduced spatter and porosity formation at a certain ring power share was often attributed to an increased keyhole opening, which also collapses and closes less frequently, resulting in a less restricted flow of metal vapor.⁵ Furthermore, a concentration of the streamlines of the flow field in the melt pool in the upper part at the rear side of the capillary was shown in the case of increased spatter generation.³

However, most studies add the additional ring intensity to that of a constant core power, or the overall power is kept constant, which leads to a change in the weld depth, resulting in a lower comparability of the process characteristics. In addition, a modified weld depth is generally not accepted in industrial applications. Furthermore, there is currently no study on how laser beam welding with FRM, especially at high-welding speeds over 10 m/min, affects process stability when welding pure nickel, a material used for many applications in the field of hydrogen production.

To further clarify the relevant effects of FRM laser welding on process dynamics and the spatter formation regime, in this study, laser beam welding tests were carried out on hidden T-joints made of 2.4068 nickel at different welding speeds as well as different intensity distributions, while maintaining a constant weld depth and monitoring the process via synchronized high-speed cameras.

II. EXPERIMENTAL SETUP

The experiments were carried out using the laser source AMB 6000/9000 (IPG Laser GmbH & Co. KG), which provides a wavelength of 1070 nm, in combination with the optical system YW52

TABLE I. Constant settings of the laser beam.

	IPG AMB 6000/9000
Laser source	9000
Wavelength	1070 nm
Fiber diameter	
Core	100 μm
Inner ring	130 μm
Outer ring	300 μm
Ratio between the focal length of the focusing lens and the collimating lens	1:2
Measured focal diameter	
Core	188 μm
Inner ring	248 μm
Outer ring	564 μm
Measured beam parameter product	
Core	3.9 mm mrad
Ring	11.6 mm mrad
Measured Rayleigh length	
Core	2.3 mm
Ring	8.0 mm
Angle of incidence	0°
Focal plane on the sheet surface	0 mm

including the IDM (Precitec GmbH & Co. KG) for optical coherence tomography (OCT) based measurements of the weld depth. The laser fiber core diameter was specified as 100 μm , the inner ring diameter was 130 μm , and the outer ring diameter was 300 μm , which, with the 1:2 ratio between the focal length of the focusing lens and the collimating lens, resulted in a measured core diameter of 188 μm , a measured inner ring diameter of 248 μm , and a measured outer ring diameter of 564 μm (measured with a MSM + HBHP by Primes GmbH). The settings and properties of the laser source used in this study can be seen in Table I and Fig. 1.

To investigate the influence of different laser beam intensity distributions on process dynamics, welding experiments in hidden-T configuration were carried out using 2.4068 nickel as

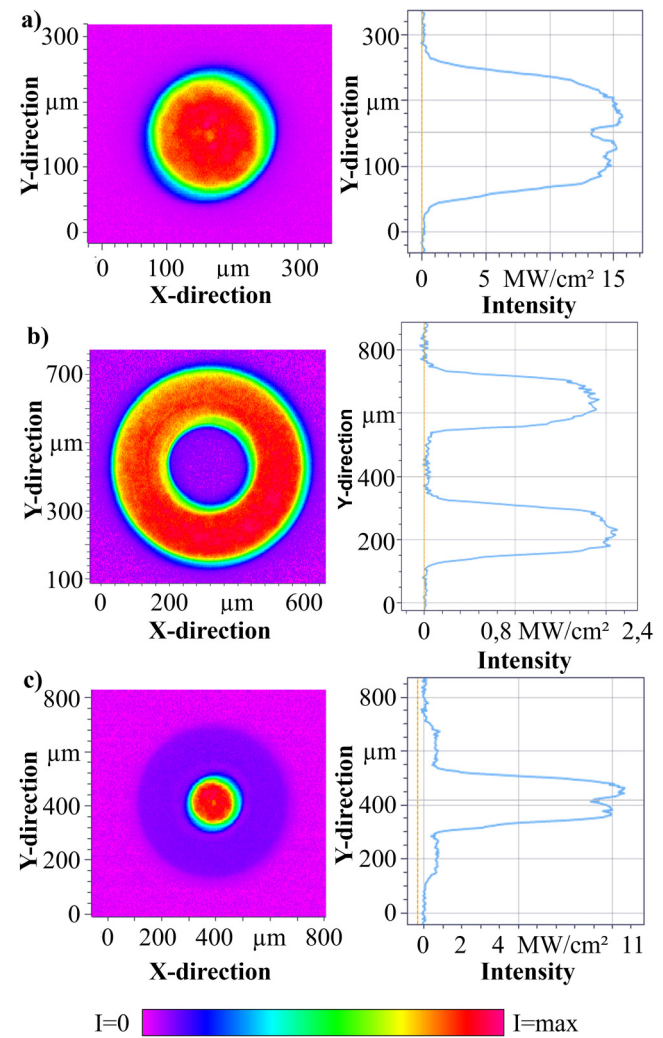


FIG. 1. Measured intensity profiles in the focal plane of the used laser beam. (a) 4000 W core, (b) 4000 W ring, and (c) 2800 W core and 1200 W ring; measured with MSM + HBHP (Primes GmbH).

26 March 2025 14:37:02

TABLE II. Chemical composition of 2.4068 nickel (wt. %) (Ref. 10).

Ni	Mn	Si	Fe	Co	C
Bal.	0.25	0.16	0.07	0.02	0.01

sample material, the composition of which is given in Table II and which was previously cleaned using ethanol.

The size of the specimen and the experimental welding setup are given in Fig. 2. Both sheets had a length of 125 mm and a width of 50 mm, with the upper sheet having a thickness of 0.8 mm and the lower sheet 1.5 mm. The samples were placed in a clamping device on a stage for process movement, which provided a constant welding speed (WS) over a seam length of 110 mm. The angle of incidence of the processing setup was set to 0°. Argon was used as shielding gas with a flow rate of 9 l/min and a nozzle diameter of 7 mm. For process monitoring, two high-speed video cameras for spatter tracking and tracking of the keyhole opening area were used in combination with a CAVILUX HF (Cavitar Ltd.) laser source, which illuminated the process zone (see Fig. 2). High-speed camera 1, the i-Speed7 (iX Cameras Ltd.) with an AF 180 mm 3.5 Di LD Macro 1:1 SP lens (TAMRON Europe GmbH) and a connected BN810 narrow near-IR bandpass filter was used for spatter tracking with a frame rate of 30 kHz and a resolution of 600 × 600 pixel (0.019 mm per pixel). It was positioned 90° to the welding direction and at a 0° tilt angle so that an image section of about 11 × 11 mm² around the process zone could be captured. The keyhole opening area was tracked by using the second

high-speed camera FASTCAM NOVA S12 (Photron) with a 12× zoom lens system (Navitar, Inc.) and a connected BN810 narrow near-IR bandpass filter operating at a frame rate of 30 kHz and a resolution of 640 × 640 pixels (0.005 mm per pixel). It was positioned opposite the welding direction and in a 55° tilt angle so that an image section of about 3.2 × 3.2 mm² around the keyhole opening could be captured. Both the spatter and the keyhole opening area were tracked by means of a brightness threshold using MATLAB-based algorithms, which were described in Ref. 11. The size of the keyhole opening area, the number of spatter, and the size of each spatter in square millimeter are outputs for each frame. Assuming that the spatters are spherical, the spatter volume was calculated. The total spatter amount was determined by multiplying the average spatter volume by the average number of spatter per second. The smallest detectable spatter size depends on the resolution and, thus, corresponds to a spatter diameter of approximately 0.02 mm.

The experimental program is presented in Table III. In the series of tests, the influence of different intensity distributions between the ring and the core as well as three different welding speeds of 8, 12, and 16 m/min on the process behavior was investigated, while keeping a constant weld depth of 1.7 mm. The power share between the ring and the core was changed by 20%. In the first step, the required total power for each distribution was determined by measuring the weld depth using OCT and adjusting the total power with the same distribution until the target of 1.7 mm was reached. In further experiments, OCT was used to monitor the weld depth. Each parameter was repeated five times to determine mean values and standard deviations.

The cross sections of each seam were taken 25 mm behind the sheet edge (see Fig. 2, A-A), polished, and etched by immersion etching for 10 s in a solution of 75 ml water, 75 ml hydrochloric acid, and 12.5 g copper sulfate. The metallographic analysis was used to validate the weld penetration depth measured by OCT and to determine the seam shape. The 80 mm-long remainder of the sample with a seam length of approximately 72.5 mm was then examined for porosity using computed tomographic x-ray analysis (CT) with a resolution of 55 μm to determine the average number and size of the pores, using the five replicated samples. Average porosity percentages independent of the weld seam width were then acquired by relating the calculated total porous volume to the resulting volume of 72.5 mm seam length, a sheet width of 1.5 mm, and a depth of 2 mm, also based on the five replicated samples.

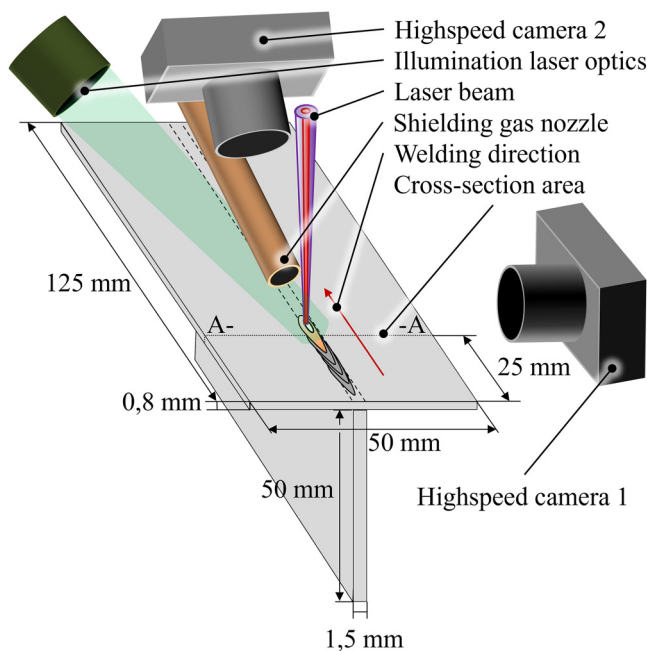


FIG. 2. Sample dimensions and a schematical experimental setup.

TABLE III. Experimental plan.

Welding speed (m/min)	Ring power share (RPS) (%)						Weld depth (mm)
	0	30 ^a	40	60	80	100	
8	0	— ^a	40	60	80	100	1.7
12	0	30 ^a	40	60	80	100	1.7
16	0	25 ^a	40	60	80	— ^a	1.7

^aDue to the minimum and maximum power of the laser source, not every power share could be used. In these cases, the closest possible distribution was applied.

26 March 2025 14:37:02

III. RESULTS

A. Weld geometry

Figure 3(a) shows the total laser power required to achieve a constant weld depth of 1.7 mm as a function of the ring power share (RPS), while in Figs. 3(b) and 3(c), the specific required laser power by the core and the ring intensity are displayed. It can be seen that the total required laser power resembles a sigmoid function for 8 and 12 m/min, while for 16 m/min, this can only be assumed, as the ring power required for 100 % ring exceeds the maximum ring power of the laser source. For up to 60 % ring power share, the required core laser power decreases slightly for 8 m/min welding speed, whereas it initially remains constant at 12 m/min and then increases slightly at 16 m/min. Above 60 %, the required core power drops significantly for all welding speeds. The required ring power increases over the ring power share in all cases, while with increasing welding speeds, the curve progresses from an approximately linear to a more exponential gradient.

The actual achieved weld depth, measured by means of metallographic cross sections, is shown in Fig. 4. The values of the average welding depth vary between 1.63 mm (12 m/min, 0 % ring power share) and 1.86 mm (12 m/min, 100 % ring power share), which are considered sufficiently accurate for the following evaluations and the reference to an approximately equal weld depth.

The metallographic cross sections are displayed in Fig. 5, assigned to the corresponding welding speed and power distribution. The observations that can be made are similar across all the speeds examined. For 0 % ring power share, the melted material is more I-shaped and only has a seam width to connection width ratio of approximately 1.7 [see Fig. 6(a)]. Whereas at 8 m/min, the metallographic cross sections reveal excess weld metal, and 12

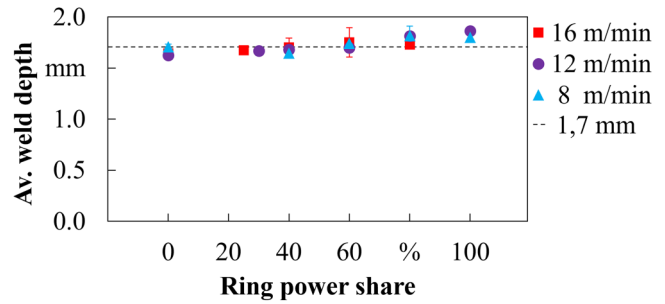


FIG. 4. Achieved weld depth measured by means of metallographic cross sections.

and 16 m/min incompletely filled grooves can be seen [see Figs. 5 and 7(b)]. Subsequently, the seam width to connection width ratio increases in all cases but with decreasing welding speed to a higher ring power share. This results in a more Y-shaped seam up to only 25 % at 16 m/min, up to 40 % at 12 m/min, and up to 60 % at 8 m/min (see Figs. 5 and 6). In this area, the seams also show higher excess weld metal values, with no significant incompletely filled grooves or seam undercuts (see Fig. 7). With an increasing ring power share, the seam width to connection width ratio decreases in all cases, resulting in I- and V-shaped seams with decreasing excess weld metal but increasing seam undercuts (see Figs. 5 and 7). With a higher ring power share, low welding speed, and seams that are not exactly centered, cross sections can sometimes be seen where the seams are inclined toward the edge of the sheet (compare Fig. 5).

B. Porosity

Representative CT scans of the welded samples are displayed in Fig. 8 and the results from the CT-based porosity analysis, averaged over five scans, can be seen in Fig. 9. Figure 9(a) shows a significant decrease in the average number of pores with an increasing ring power share for all welding speeds, whereby the average number of pores is the highest at a low ring power share for 8 m/min and decreases with an increasing welding speed. The average pore volume, on the other hand, seems to increase with the increasing ring power share, especially for 8 and 12 m/min. This can also be seen in the representative CT scans. However, it should be noted that these trends have a high standard deviation. For 16 m/min, the average pore volume increases slightly up to around 60 % ring power share and then decreases again. The overall porosity [Fig. 9(c)] decreases over the increasing ring power share in the case of 8 m/min, whereas at 12 m/min and 16 m/min, between 40 % and 60 % ring power, a maximum porosity is recognizable, after which the porosity drops again in both cases. For 12 m/min, the trend underlies a high standard deviation.

C. Keyhole and spatter analysis

The keyhole opening area shape, as well as the formation source and mechanism of the spatter depending on the ring power share for the welding speed of 16 m/min, can be concluded from Fig. 10, which shows representative frames from high-speed videos from the side (camera 1, Fig. 2) and top views (camera 2, Fig. 2) at

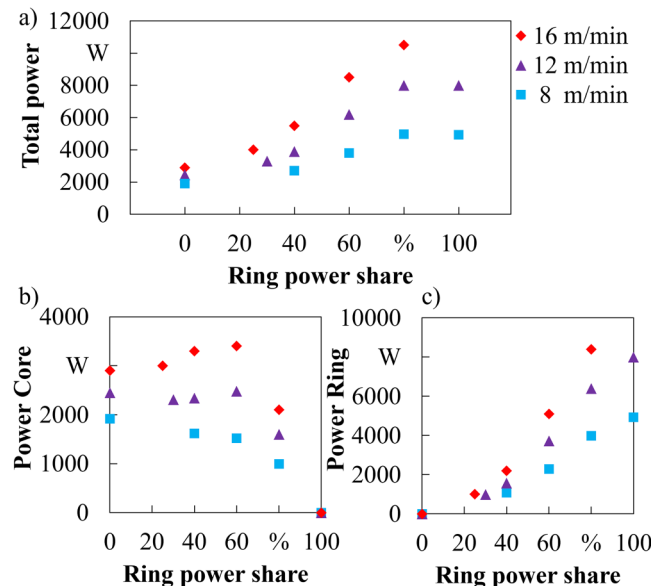


FIG. 3. Required laser power as a function of the ring power share to achieve a constant weld depth of 1.7 mm.

26 March 2025 14:37:02

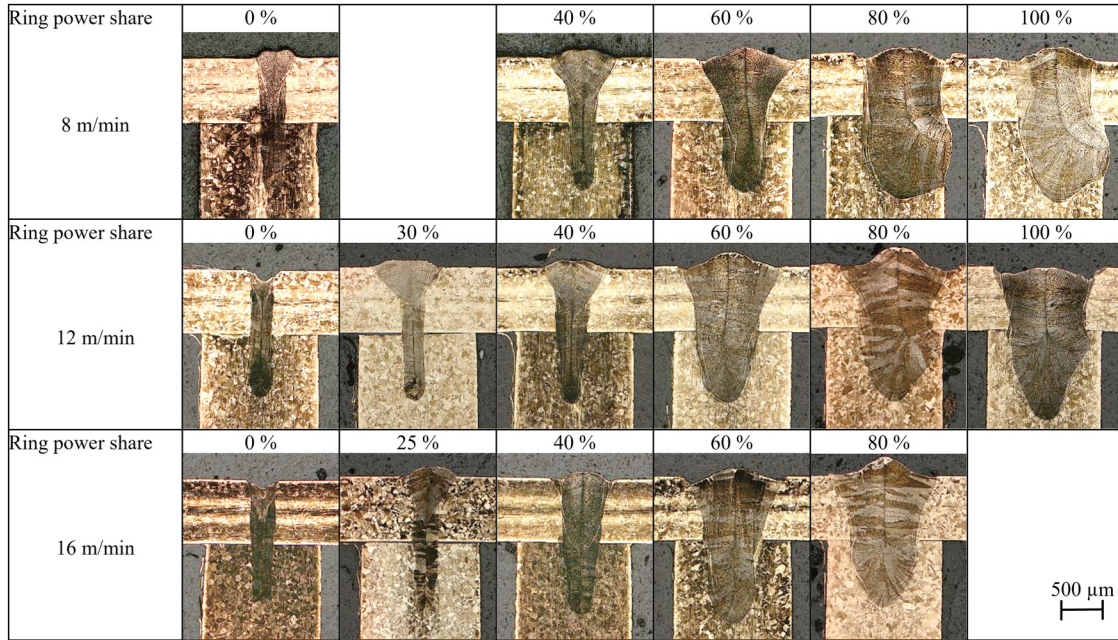


FIG. 5. Characteristic cross sections in dependence on the power distribution between the core and the ring at welding speeds of 8, 12, and 16 m/min.

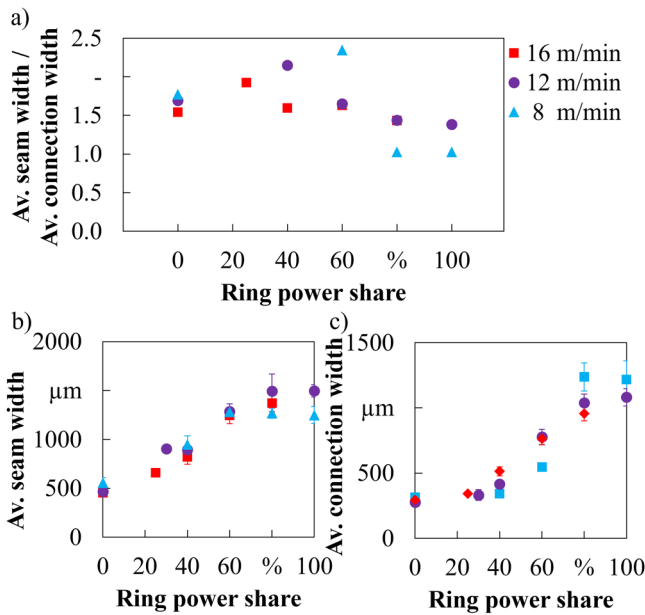


FIG. 6. (a) Ratio of average seam width and average connection width; (b) average seam width; and (c) average connection width; all diagrams over ring power shares; the values are based on metallographic cross sections.

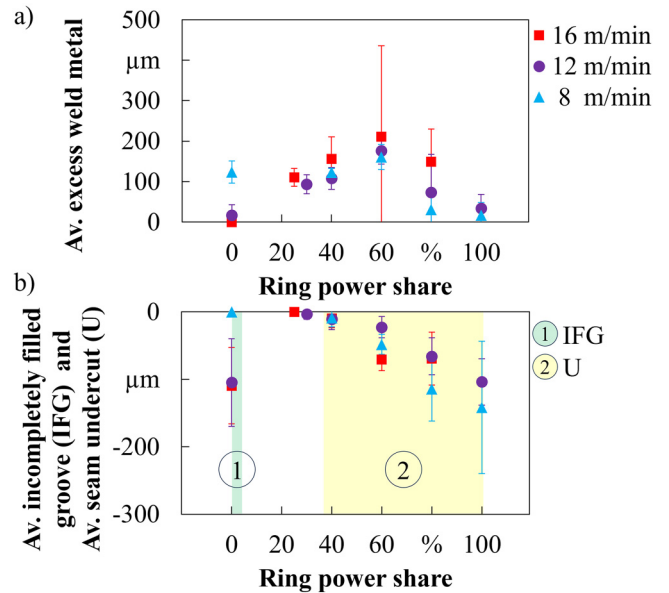


FIG. 7. (a) Average excess weld metal measured from cross sections. (b) Average incompletely filled groove (IFG) and average seam undercut measured from cross sections; all over ring power shares and based on metallographic cross sections.

26 March 2025 14:37:02

WS (m/min)	RPS (%)	Representative CT-scan
8	0	
	40	
	60	
	80	
	100	
12	0	
	30	
	40	
	60	
	80	
	100	
16	0	
	25	
	40	
	60	
	80	

FIG. 8. Representative longitudinal CT scans in dependence on the RPS at WS of 8, 12, and 16 m/min.

the same time. At 0% ring power share, the keyhole opening area appears round. Spatters form at the back of the keyhole by separating from a periodically up-and-down swelling melt pillar. At 40% ring power share, the melt pillar at the back of the round keyhole area is much smaller and only very few spatters can be detected. For 80% ring power share, the keyhole opening area appears to be elongated and a different spatter formation area can be identified. Melt swellings and detaching spatter form on the sides of the keyhole instead of its rear. For the welding speeds of 8 and 12 m/min, the same effects are observed, but the transitions shift to slightly higher ring power shares at 8 m/min.

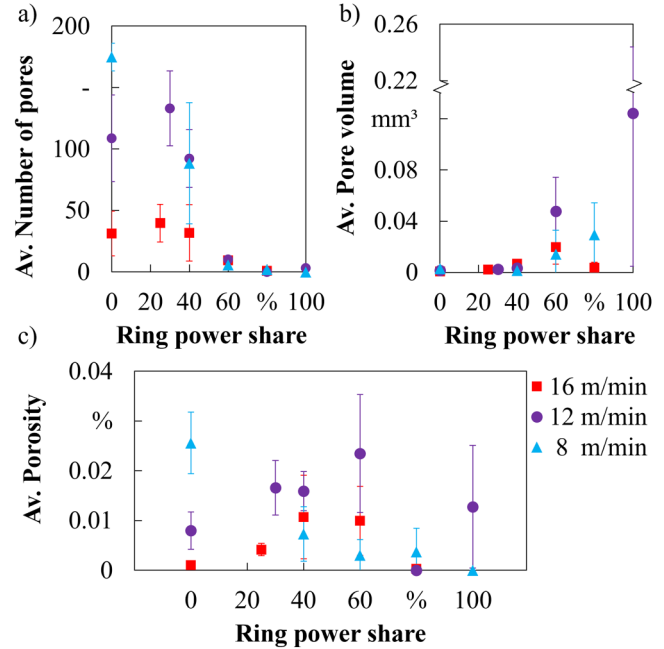


FIG. 9. (a) Average number of pores; (b) average pore volume; and (c) average porosity; all over ring power shares and based on CT analysis.

The average keyhole opening area determined by means of MATLAB-based analysis of each frame of the high-speed videos from the top view (see Fig. 10) is shown in Fig. 11. For all welding speeds investigated, the average keyhole opening area increases significantly with an increasing ring power share. The gradient of the increase rises with an increasing welding speed, which means that, at 80% ring power share, the keyhole opening area is 0.496 mm² for 8 m/min, 0.920 mm² for 12 m/min, and 1.434 mm² for 16 m/min. For 8 and 12 m/min, a maximum keyhole opening area is formed above 80% ring power share, which cannot be confirmed for 16 m/min, because the 100% ring power share could not be achieved due to the maximum ring power of the laser source. In addition to the average keyhole opening area, its standard deviation also increases significantly for all welding speeds with the increasing ring power share [see Fig. 11(b)]. For this reason, the ratio of the two values was also calculated and is shown in Fig. 11(c). A significant decrease in the ratio from 0% ring power share to around 60% ring power share can be seen here. As the ring power share increases further, the ratio increases very slightly at all welding speeds investigated.

Figure 12 shows the influence of the ring power share on the average number of spatters per second (a), the average spatter volume (b), and the resulting average total spatter amount (c), all determined by means of MATLAB-based analysis of the high-speed videos from camera 1 (side view). With an increasing ring power share, a significant decrease in the average number of spatters per second up to a certain ring power share can be observed for all investigated welding speeds, whereas the values for 12 and 16 m/min begin considerably higher than those for 8 m/min at 0% ring power share. After the minimum at 60% for 8 m/min and 40% for

26 March 2025 14:37:02

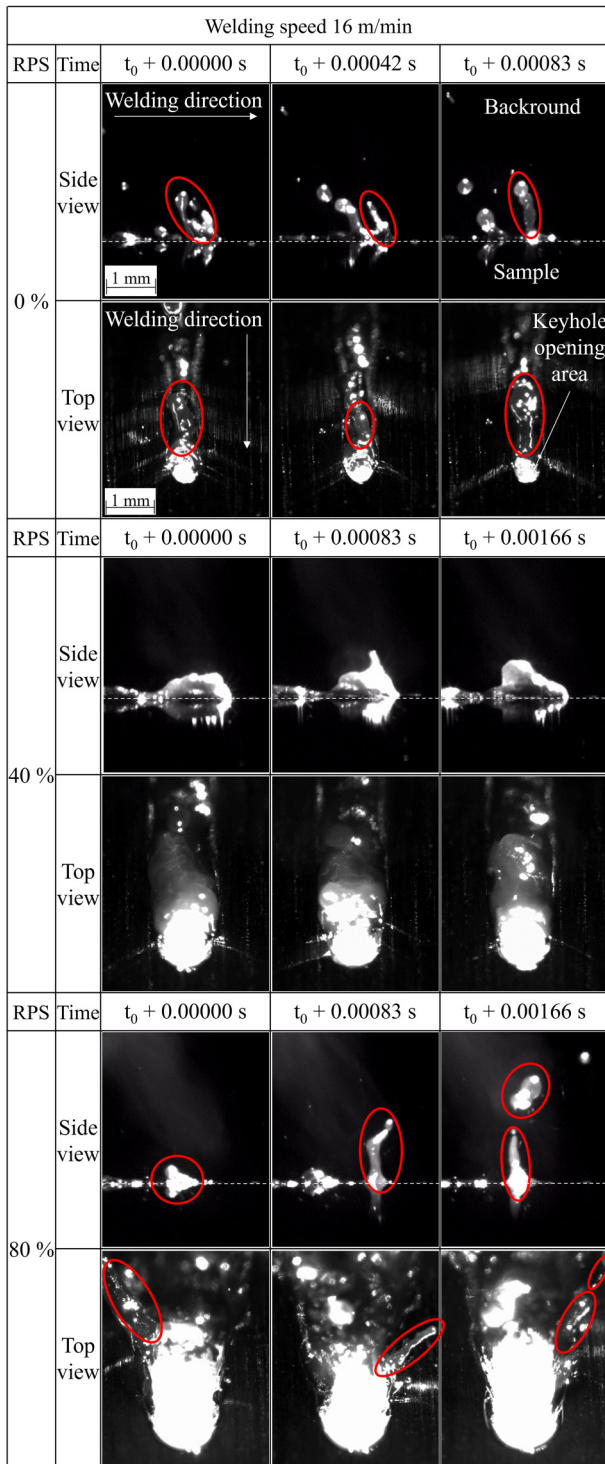


FIG. 10. Representative frames from a high-speed video from different positions at the same time, showing the most frequent type of spatter formation at a welding speed of 16 m/min and ring power shares of 0 %, 40 %, and 80 %.

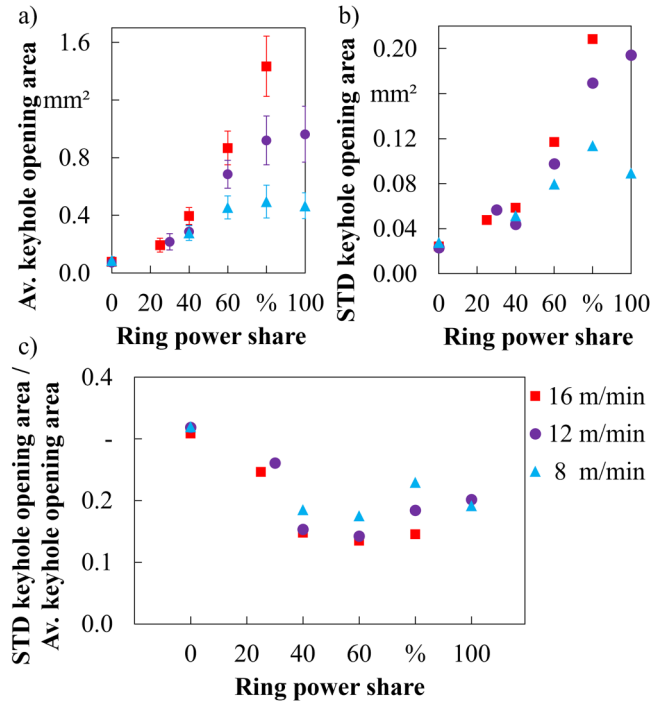


FIG. 11. (a) Average keyhole opening area determined by means of MATLAB-based analysis of the high-speed videos from camera 2 (top view); (b) standard deviation of the keyhole opening area; and (c) ratio between the standard deviation of the keyhole opening area and the actual average keyhole opening area.

26 March 2025 14:37:02

12 m/min and 16 m/min, the values for 8 m/min remain constant, whereas the average number of spatters per second for 12 and 16 m/min increases significantly. The average spatter volume remains rather constant over the ring power share for 8 m/min, whereas 12 and 16 m/min show a minimum of about 40 %, similar to the average number of spatters per second, which is less significant due to the high standard deviations. The average total spatter amount, given in Fig. 12(c), shows a low spatter amount for 8 m/min across all ring power shares. For 12 and 16 m/min, it can be seen that a high spatter amount occurs at 0 % RPS, which falls to a minimum at 40 % with increasing ring power shares and then increases significantly.

IV. DISCUSSION

The progression of the required core power over the increasing ring power share for a constant weld depth (Fig. 3) shows that, due to the almost constant core power up to around 60 %, the welding depth up to this point is mainly caused by the core power and the increasing ring power share has no major influence on the weld depth. The reason for this is the relatively low intensity at 60 % ring power due to the significantly larger cross-sectional area of the ring beam (see Fig. 1), and this has already been shown in studies for other materials like aluminum.⁵

However, the drop in the ratio of seam width and connection width (Fig. 6) for all welding speeds, as well as the changing shape of

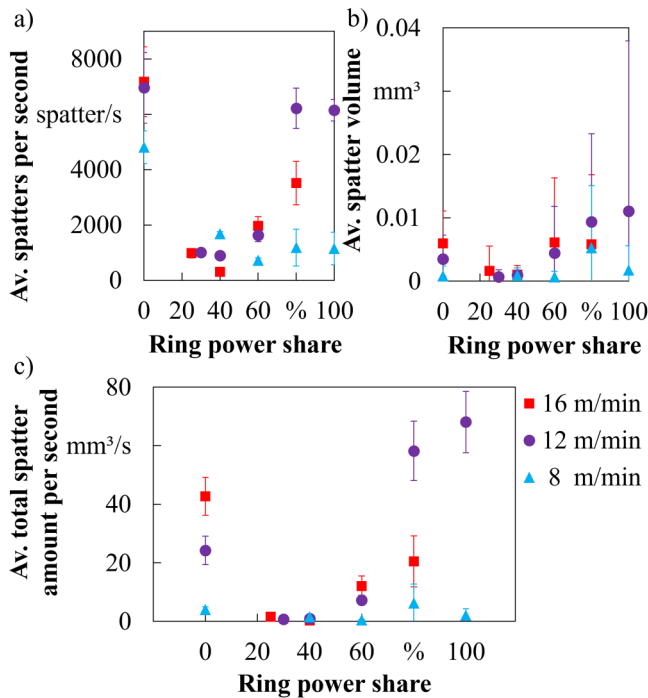


FIG. 12. Influence of the ring power share on the average number of spatters per second (a), the average spatter volume (b), and the average spatter amount resulting from the multiplication of the two factors (c) determined by means of MATLAB-based analysis of the high-speed videos from camera 1 (side view).

the seam cross sections from an I- to a Y- and then to a V-shaped seam, shows that the increasing ring power share affects the shape of the keyhole. The increasing ring power share initially affects the upper part of the keyhole by widening it at the top, while the connection width remains the same at first (Y-shaped cross section and peak in seam width/connection width ratio). This effect was also shown in other studies and often linked to a reduction of spatter and porosity.⁵ As the intensity increases, the ring power share has an increasing effect on deeper areas of the keyhole and finally creates the V-shaped form of the cross section at 100 % ring power share. The decreasing peak in seam width/connection width ratio with the increasing welding speed and the drop after the peak, which can be observed with increasing welding speeds at lower ring power shares, shows that the effect of enlarging the keyhole opening decreases with the increasing welding speed and is shifted to lower ring power shares.

When welding too close to the edge with high ring power shares and lower welding speed, slightly curved seams occur at one side, probably as the keyhole inclines toward the wall due to the reduced possibility of heat dissipation through heat conduction as a result of the thinner wall thickness (see Fig. 5).

From the high-speed recordings, three different process regimes or characteristics can be identified in line with the three different characteristics of the spatter quantity (many spatters with no ring power share, minimum spatter quantity with a certain ring power share, and increase in spatter quantity with a further increase in ring power share): The first process regime with no or little additional ring power share is the “single wave regime” according to Fabbro *et al.*, which is

characterized by a large single swelling near the top of the rear keyhole wall and spatter emitting from that region (see Fig. 10).² The swelling and the amount of spatter that detaches there then initially decreases with an increasing ring power and leads to the formation of a regime with a relatively stable keyhole dynamic, which can be concluded from the low ratio of standard deviation of the keyhole area to the average keyhole area [see Figs. 10 and 11(c)]. With further increasing the ring power share to over 60 %, the mechanism of spatter formation changes fundamentally for all welding speeds used (see Fig. 10) and the process resembles the “elongated keyhole regime.”² Beside the clearly elongated keyhole area, the swellings and detaching spatter are no longer observed at the rear wall but are lateral on both sides of the keyhole. This change in the spatter formation mechanism, in combination with the only slightly increased keyhole opening at 16 m/min, shows that, in addition to an improvement in the gas flow due to an increased keyhole opening, the increasing ring power share also changes the melt flow from a jet directed upward on the keyhole back wall to a jet directed upward along the sidewalls of the keyhole, suppressing each other if the power share is selected appropriately. However, since Fabbro *et al.* detected only a small amount of spatter in this regime,² we assume that the ring intensity intensifies the upward melt flow along the sidewalls of the keyhole.

This influence of the ring power share on the melt flow and the changing spatter formation mechanism is supported by the results of incompletely filled grooves and seam undercuts [Fig. 7(b)]. The massive loss of mass due to the spatter from the keyhole rear wall at 0 % ring power share [see Fig. 12(c)] can be seen in the cross sections of the seam as incompletely filled grooves. A ring power share of approximately 40 % and the associated improved melt flow, resulting in the low total spatter amount, leads to the formation of a cross section without incompletely filled grooves and seam undercuts at all welding speeds. The loss of mass due to the total spatter amount above 60 % ring power share [see Fig. 12(c)], which occurs on the side of the keyhole, is noticeable in the form of seam undercuts at the edges of the seam (see Fig. 7).

The porosity also shows the three regimes. At 0 % ring power share, small pores can be found as a result of the high ratio of the standard deviation of the keyhole area to the average keyhole area, as well as the number of spatters, which both indicate an unstable keyhole. With an increasing ring power share, it was previously shown that the proportion of smaller pores decreases, while a few larger pores appear. This is attributed to the stabilized keyhole dynamics and improved degassing via the enlarged keyhole and the enlarged melt pool as a result of the increased power and laser beam cross-sectional area. At high ring power shares of over 60 %, no or very few large pores occur, as the possibility of degassing is significantly improved, but process instabilities have a greater impact due to the significant increase in power. The reduction in the average number of pores with a simultaneous increase in the average pore size points to the fact that the total proportion of porosity could not be significantly reduced in 2.4068 nickel using an FRM laser source.

In summary, the three identified regimes are characteristically plotted in Fig. 13 over the ring power share and the welding speed: the already known “single wave regime” as well as the “stabilized regime” and “lateral spatter regime.” It should be noted that the transitions between these regimes are not sudden but smooth and that lower or higher welding speeds will possibly lead to different characteristics, for example as a result of humping.

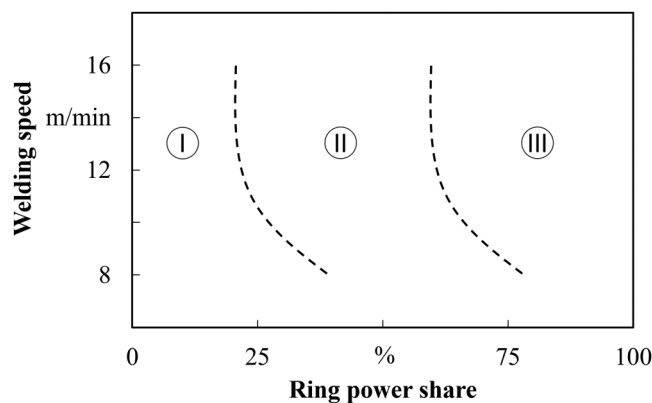


FIG. 13. Process regimes of laser beam welding of nickel 2.4068, depending on the ring power share and welding speed; I: single wave regime (Ref. 2), II: stabilized regime, and III: lateral spatter regime. It should be noted that the transitions between the regimes are not sudden but smooth.

V. CONCLUSION

In this study, laser beam deep penetration welding tests were carried out on hidden T-joints of 2.4068 nickel using an infrared flexible ring mode laser source. While keeping a constant weld depth, three different welding speeds ranging from 8 to 16 m/min were applied with different ring power shares ranging from 0 % to 100 % to determine their influence on process dynamics and seam properties, which were detected using high-speed videos, metallographic analyses, and CT scans.

Four main conclusions can be drawn as follows:

- (1) When welding with FRM laser sources, three different process regimes can be identified depending on the ring power share and the welding speed: The well-known “single wave regime,” the “stabilized regime,” and the “lateral spatter regime.”
- (2) An additional ring power share changes the melt flow along the keyhole and thus the formation mechanism of the occurring spatter.
- (3) An adapted distribution of ring and core intensity can, therefore, reduce the amount of spatter, the number of pores, and the formation of incompletely filled grooves for 2.4068 nickel at all investigated welding speeds compared with welding with 100 % core power share.
- (4) The welding speeds investigated have no significant influence on the change in melt flow due to the additional ring content.

ACKNOWLEDGMENTS



The project on which this report is based was funded by the German Federal Ministry of Education and Research under Funding No. 03HY119F. The responsibility for the content of this publication lies with

the authors.

AUTHOR DECLARATIONS

Conflict of Interest

The authors have no conflicts to disclose.

Author Contributions

Marcel Möbus: Conceptualization (lead); Data curation (lead); Formal analysis (lead); Funding acquisition (equal); Investigation (lead); Methodology (lead); Project administration (lead); Resources (lead); Software (equal); Validation (lead); Visualization (lead); Writing – original draft (lead); Writing – review & editing (equal). **Ronald Pordzik:** Conceptualization (supporting); Software (equal); Writing – review & editing (equal). **Thomas Seefeld:** Supervision (lead); Writing – review & editing (equal).

DATA AVAILABILITY

The data that support the findings of this study are available from the corresponding author upon reasonable request.

REFERENCES

- ¹M. Wappler, D. Ungeder, X. Lu, H. Ohlmeyer, H. Teschke, and W. Lueke, “Building the green hydrogen market—Current state and outlook on green hydrogen demand and electrolyzer manufacturing,” *Int. J. Hydrogen Energy* **47**, 33551–33570 (2022).
- ²R. Fabbro, S. Slimani, F. Coste, and F. Briand, “Analysis of the various melt pool hydrodynamic regimes observed during cw Nd-YAG deep penetration laser welding,” in *International Congress on Applications of Lasers & Electro-Optics*, Orlando, FL, October 29–November 1, 2007 (Laser Institute of America, Orlando, 2007), p. 802.
- ³M. Jarwitz, J. Lind, R. Weber, T. Graf, N. Speker, and P. Haug, “Investigation of the influence of superimposed intensity distributions on the spatter behavior in laser welding of steel using online x-ray diagnostics,” in *Proceedings of the 37th International Congress on Applications of Lasers & Electro-Optics (ICALEO 2018)*, Orlando, FL, October 14–18, 2018 (Laser Institute of America, Orlando, 2018).
- ⁴Z. Wang, M. Jiang, X. Chen, Y. Du, Z. Lei, S. Zhao, and Y. Chen, “Mitigating spatters in keyhole-mode laser welding by superimposing additional ring-shaped beam,” *Opt. Laser Technol.* **168**, 109869 (2024).
- ⁵E. Punzel, F. Hugger, T. Dinkelbach, and A. Bürger, “Influence of power distribution on weld seam quality and geometry in laser beam welding of aluminum alloys,” *Proc. CIRP* **94**, 601–604 (2020).
- ⁶Y. Zhang, J. Chen, W. Zhang, C. Li, C. Qiu, J. Ding, H. Lu, and K. Zhang, “Study of spatter net forming mechanism and penetration mode under flexible ring mode laser welding,” *J. Mater. Res. Technol.* **24**, 2213–2225 (2023).
- ⁷W. Xie, J. Wang, F. Lyu, X. Li, B. Xu, P. Zhang, and X. Zhan, “Investigation on keyhole stability and surface quality in laser welding of TC4 titanium alloy with adjustable ring-mode (ARM) laser,” *Int. J. Adv. Manuf. Technol.* **130**, 1307–1320 (2024).
- ⁸T. Sun, S. Jabar, N. Kumar, C. Liu, D. Ceglarek, and P. Franciosa, “The impact of ring-shaped laser beam on dissimilar welding of Al-Cu thin sheets for battery tab-to-busbar connection microstructural, mechanical and electrical characteristics,” *Opt. Laser Technol.* **179**, 111312 (2024).
- ⁹F. Kaufmann, A. Maier, J. Schrauder, S. Roth, and M. Schmidt, “Influence of superimposed intensity distributions on weld seam quality and spatter behavior during laser beam welding of copper with green laser radiation,” *J. Laser Appl.* **34**(4), 042008 (2022).
- ¹⁰Nippon Yakin Kogyo Co., LTD, “Kawasaki Plant: Inspection Certificate,” No. 19EA-047315 B, 2019.
- ¹¹M. Möbus, R. Pordzik, A. Krämer, T. Mattulat *et al.*, “Process comparison of laser deep penetration welding in pure nickel using blue and infrared wavelengths,” *Weld. World* **68**, 1473–1484 (2024).

26 March 2025 14:37:02